Geophys. J. Int. (2003) **152,** 699–717

A shallow fault-zone structure illuminated by trapped waves in the Karadere–Duzce branch of the North Anatolian Fault, western Turkey

Yehuda Ben-Zion,[1] Zhigang Peng,[1] David Okaya,[1] Leonardo Seeber,[2] John G. Armbruster,[2] Naside Ozer,[3] Andrew J. Michael,[4] Serif Baris[5] and Mustafa Aktar[5]

[1] *Department of Earth Sciences, University of Southern CA, Los Angeles,* CA 90089-0740, *USA. E-mail: benzion@terra.usc.edu*
[2] *Lamont-Doherty Earth Observatory, Palisades,* NY 10964, *USA*
[3] *The University of Istanbul, Geophysical Engineering Department* 34850, *Avcilar, Istanbul*
[4] *United States Geological Survey, MS* 977, 345 *Middlefield Rd, Menlo Park,* CA 94025, USA
[5] *Kandilli Observatory and Earthquake Research Institute of Bogazici University,* 81220 *Cengelkoy, Istanbul*

Accepted 2002 October 2. Received 2002 September 18; in original form 2002 June 17

SUMMARY

We discuss the subsurface structure of the Karadere–Duzce branch of the North Anatolian Fault based on analysis of a large seismic data set recorded by a local PASSCAL network in the 6 months following the $M_w = 7.4$ 1999 Izmit earthquake. Seismograms observed at stations located in the immediate vicinity of the rupture zone show motion amplification and long-period oscillations in both *P*- and *S*-wave trains that do not exist in nearby off-fault stations. Examination of thousands of waveforms reveals that these characteristics are commonly generated by events that are well outside the fault zone. The anomalous features in fault-zone seismograms produced by events not necessarily in the fault may be referred to generally as fault-zone-related site effects. The oscillatory shear wave trains after the direct *S* arrival in these seismograms are analysed as trapped waves propagating in a low-velocity fault-zone layer. The time difference between the *S* arrival and trapped waves group does not grow systematically with increasing source–receiver separation along the fault. These observations imply that the trapping of seismic energy in the Karadere–Duzce rupture zone is generated by a shallow fault-zone layer. Traveltime analysis and synthetic waveform modelling indicate that the depth of the trapping structure is approximately 3–4 km. The synthetic waveform modelling indicates further that the shallow trapping structure has effective waveguide properties consisting of thickness of the order of 100 m, a velocity decrease relative to the surrounding rock of approximately 50 per cent and an *S*-wave quality factor of 10–15. The results are supported by large 2-D and 3-D parameter space studies and are compatible with recent analyses of trapped waves in a number of other faults and rupture zones. The inferred shallow trapping structure is likely to be a common structural element of fault zones and may correspond to the top part of a flower-type structure. The motion amplification associated with fault-zone-related site effects increases the seismic shaking hazard near fault-zone structures. The effect may be significant since the volume of sources capable of generating motion amplification in shallow trapping structures is large.

Key words: fault models, guided waves, inversion, low-velocity zone, waveform analysis.

1 INTRODUCTION

1.1 Tectonic environment and seismic network of the Karadere–Duzce fault

The North Anatolian Fault (NAF) system is the largest geological structure in Turkey, extending for over 1600 km from its origin at the Karliova triple junction where it intersects with the East Anatolian Fault. The NAF defines the northern boundary of the Anatolian block that is extruded westward under the combined effect of Arabia–Asia convergence to the east and southwestward extension related to the Aegean subduction rollback in the west (e.g. Jackson & McKenzie 1988; Taymaz *et al.* 1991). This regime has been active for ≈5 Myr, has accumulated ≈80 km of right-lateral offset and has a current

rate of ≈2.4 cm yr^{-1} in northwestern Turkey (e.g. Sengor *et al.* 1985; Armijo *et al.* 1999a,b; Reilinger *et al.* 1997). The long- and short-term kinematic parameters of the NAF are comparable and intermediate to those of the San Andreas Fault (SAF) in California and the Dead Sea Transform in the Middle East. Morphologically, the NAF is a fairly continuous and linear structure from the Karliova triple junction to Bolu at the eastern edge of the 1999 November rupture. From there the fault splits into two major branches (Fig. 1). The northern one follows the Duzce and Karadere segments through the Adapazari basin into the sea of Marmara. The southern branch extends along the Mudurnu river valley through Pamukova and Iznik lake, and enters the sea of Marmara at the Gulf of Gemlik. Six earthquakes with $M = 7+$ have ruptured the NAF progressively from east to west beginning in 1939 (Barka 1996; Barka & Kadinsky 1988). The most recent and westernmost of these are the 1999 contiguous $M_w = 7.4$ Izmit and $M_w = 7.2$ Duzce earthquakes, which ruptured jointly several segments of the northern strand of the NAF for approximately 160 km (e.g. Barka *et al.* 2000; Toksöz 2002, and references therein).

A week after the 1999 August 17, $M_w = 7.4$ Izmit earthquake, we deployed a 10-station PASSCAL seismic network along and around the Karadere–Duzce branch of the fault (Fig. 1a). One goal of the deployment was to image the subsurface structure of the fault using seismic guided waves that propagate in low-velocity damaged fault-zone (FZ) layers. The Karadere–Duzce branch was chosen for the deployment because the rupture broke the surface there in bedrock, avoiding sedimentary layers that can diffuse and mask signals propagating in the FZ. The choice of location was fortunate because 3 months later the 1999 November 12, $M_w = 7.2$ Duzce earthquake started and propagated eastward from the Karadere–Duzce fault. The blue and purple squares in Fig. 1(a) mark, respectively, GPS locations of the surface ruptures of the large August and November events on the Karadere–Duzce branch of the NAF. As seen in the figure, our local seismic network straddles the eastern end of the August $M_w = 7.4$ rupture and the western end of the November $M_w = 7.2$ event.

In 2000 January–February we deployed 16 additional PASSCAL sensors in a tight 'T-array' (Fig. 1b) along and normal to the Karadere–Duzce branch for 14–19 days, before removing both arrays. All seismic stations in both arrays (triangles in Fig. 1) had REFTEK recorders and three-component L22 sensors. In addition, eight of the 10 longer-term stations had three-component force-balance accelerometers and sites MO (for the full deployment) and GE (for the first two months) had three-component broad-band (Guralp CMG-40T) sensors. The Karadere–Duzce fault in our study area has a strike of approximately 70° (ENE) and it follows a steep and narrow valley. The inclined (rather than more perpendicular) lines made by the T-array sites across the fault reflect the steep topography in the region. The configuration of the longer-term network was a compromise between monitoring ray-paths along and near the fault and having sufficient aerial coverage for determination of event locations and regional velocity structure. Near the surface trace of the August rupture, the station spacing ranges from tens of metres in the across-fault line of the T-array to hundreds of metres along the fault. Our Karadere–Duzce seismic network recorded in a trigger mode over 26 000 events, including many thousands of waveforms that propagated within and around the damaged fault-zone material. Additional details on the deployment and initial results on seismicity, waveform character and seismotectonic interpretation can be found in Seeber *et al.* (2000a).

As noted above, the Karadere–Duzce fault is at the transition between the roughly linear central portion of the NAF and the western part where the fault system bifurcates. In the simpler central part, the motion appears to be purely right-lateral and is accommodated by relatively few and large strike-slip earthquakes with low interseismic activity. In the western multibranched portion, the plate motion is oblique to the NAF and includes an extensional component (e.g. Reilinger *et al.* 1997). The background seismicity in western Turkey is high, diffused, and includes many earthquakes with dominant normal dip-slip (e.g. Jackson & McKenzie 1988). The geometry, scale, plate motion and seismic activity of the Karadere–Duzce branch of the NAF resemble those of the SAF system in southern California as it approaches the oceanic ridge transform in the Gulf of California. Our study area on the western NAF also shares a similar geometry and scale with the region west of San Francisco that includes the San Andreas and San Gregorio faults, the Dead Sea Transform in the southern Arava valley and north of the sea of Galilee, and the southern Alpine fault near Wellington New Zealand. The imaging results of the present study are likely to be relevant to those and other large continental strike-slip faults.

1.2 A brief background on seismic fault-zone guided waves and main results

Damaged (cracked) FZ layers and other low-velocity structures with spatially persistent material interfaces (separating regions of different elastic properties) can generate seismic guided head and trapped waves indicative of their velocity structure. Fault-zone *P* and *S* head waves are seismic disturbances that propagate along material interfaces in the FZ with the velocity and motion polarity of the body waves on the faster side of the interface. These phases are analogous to head waves in horizontally layered media. They arrive at near-fault stations in the slower-velocity medium before the direct body waves and are characterized by an emergent waveform having reversed first-motion polarity from that of the direct arrivals. Fault-zone trapped waves are slow seismic energy associated with constructive interference of critically reflected phases propagating within low-velocity FZ layers. For the *SH* case they are analogous to surface Love waves in a horizontally layered structure. They arrive after the head, direct and early scattered waves and are characterized by large-amplitude oscillations, which develop dispersion with propagation distance in the waveguide and have a lower-frequency content than the body waves. Ben-Zion & Aki (1990) and Ben-Zion (1998) give detailed descriptions of theoretical properties of these waves in ideal 2-D homogeneous seismic waveguides. Leary *et al.* (1991), Huang *et al.* (1995), Li & Vidale (1996), Igel *et al.* (1997, 2002), Fohrmann *et al.* (2001, 2002) and Jahnke *et al.* (2002) discuss properties of guided waves in irregular 2-D and 3-D FZ structures. Igel *et al.* (2002) and Fohrmann *et al.* (2001, 2002) showed that a shallow FZ layer can trap seismic energy generated by events that are deeper and well outside it. In contrast, the generation of trapped waves in a homogeneous or smoothly varying FZ layer that spans the depth extent of seismicity requires sources that are within or very close to the FZ. These results play an important role in our interpretation of trapped waves in the Karadere–Duzce branch of the NAF.

Fukao *et al.* (1983) and Hori *et al.* (1985) observed and performed ray-tracing calculations of FZ head and trapped waves in the subduction zone of the Philippine Sea Plate underneath Japan. Cormier & Spudich (1984) and Spudich & Olsen (2001) analysed with ray-tracing and finite-difference calculations motion amplification and waveform complexities in the San Andreas and Calaveras faults in California. Ben-Zion & Malin (1991) and Ben-Zion *et al.* (1992) observed FZ head waves in the Parkfield segment of

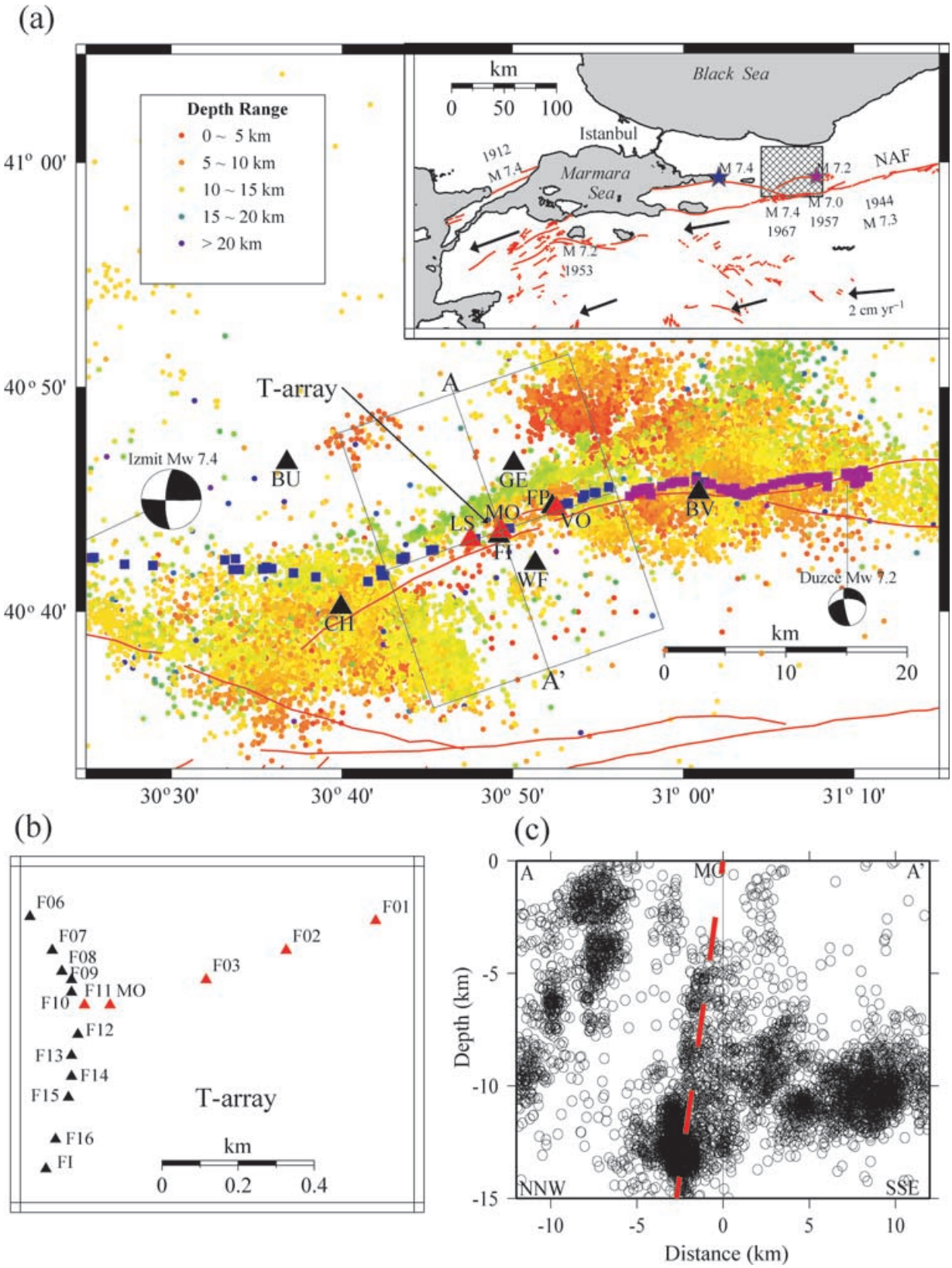

Figure 1. (a) A location map for our seismic experiment along the Karadere–Duzce branch of the NAF. The surface ruptures of the large 1999 August Izmit and 1999 November Duzce earthquakes are indicated with blue and purple squares, respectively. Seismic stations are marked by triangles. Red represents stations within a few metres from the surface expression of the Izmit rupture. Aftershock locations are marked with colours denoting different depth ranges. The inset shows the tectonic environment in northwestern Turkey with the hatched box corresponding to our study area. Red lines denote active faults with the time of latest large ruptures and arrow vectors represent the plate deformation rate from GPS data (Reilinger *et al.* 1997). (b) A location map of the dense T-array. (c) Hypocentres projected from the box in (a) along the cross-section AA′. The red dashed line indicates a steep north-dipping fault below our network.

the SAF and performed a joint traveltime tomography for head and direct *P* arrivals in that location. Hough *et al.* (1994) modelled with the solution of Ben-Zion & Aki (1990) a few waveforms with candidate head waves in the aftershock zone of the 1992 Joshua-Tree California earthquake. Shapiro *et al.* (1998, 2000) analysed with finite-difference calculations and other techniques candidate guided waves in the Middle America subduction zone near Mexico.

Fault-zone trapped waves received considerable attention following the works of Li & Leary (1990) and Li *et al.* (1994), who analysed trapped waves at the Parkfield segment of the SAF and the rupture zone of the 1992 Landers CA earthquake. Using normal-mode summation for a 1-D waveguide structure, they modelled portions of a few seismograms at each location with candidate trapped waves in terms of deep uniform FZ layers that span the entire seismogenic zone. Li *et al.* (1998, 2000) and Li & Vernon (2001) modelled with 2-D and 3-D finite-difference calculations candidate trapped waves at Landers, the rupture zone of the 1995 Kobe Japan earthquake, and the San Jacinto fault in California, using increasingly more elaborate models of deep heterogeneous low-velocity FZ layers that span the seismogenic zones at the various locations. In contrast to those results, Michael & Ben-Zion (1998, 2002) and Korneev *et al.* (2002) concluded from systematic examination of thousands of FZ waveforms that trapped waves at Parkfield are produced only or primarily by a relatively shallow and isolated low-velocity zone at a depth of approximately 3.5 km near the transition between the creeping and locked segments of the SAF. Peng *et al.* (2002a,b) analysed several hundred waveforms recorded at the rupture zone of the 1992 Landers earthquake and concluded that the trapping of seismic energy at Landers is probably also associated with a shallow FZ layer. Ben-Zion (1998) and Ben-Zion & Sammis (2003) give additional summaries of previous observation and modelling of candidate FZ guided waves.

In this work we examine thousands of seismograms recorded by our Karadere–Duzce network and find that waveforms at stations located on the Karadere–Duzce rupture zone have in general large-amplitude oscillations after the *S* arrivals compatible with expectations for FZ trapped waves. Such characteristics appear for the majority of both on- and off-fault events, and they do not exist in nearby off-fault stations. These results and traveltime analysis of hundreds of seismograms in several cross-sections along and off the fault indicate that the trapping of seismic energy in the Karadere–Duzce branch of the NAF is generated by a shallow FZ layer that persists only to a depth of a few kilometres. Synthetic waveform modelling of sets of FZ waveforms indicates that the shallow subsurface damage zone extends to a depth of approximately 3–4 km and has effective waveguide properties characterized by a thickness of the order of 100 m, a velocity decrease of approximately 50 per cent relative to the surrounding rock and an *S*-wave quality factor of 10–15. The large-motion amplification generated at FZ stations by most events implies an elevated seismic shaking hazard near similar fault zone (and other shallow trapping) structures.

2 ANALYSIS

2.1 Seismicity and waveform character

Fig. 1(a) shows locations, colour-coded by depth, of 26 400 earthquakes recorded during the operation period of our Karadere–Duzce seismic network. The locations were obtained in several stages, starting with standard HYPOINVERSE determinations (Klein 1978) and continuing with event-dependent station corrections (Seeber *et al.* 2003, in preparation). The horizontal location errors are less than 1 km near the centre of the network and 1–2 km near the margins. The vertical errors are somewhat greater. These errors are sufficiently small for the analysis performed in this work. Fig. 1(c) gives hypocentre locations projected from the box of Fig. 1(a) on a vertical plane along the cross-section AA′. In the top 10 km of the Karadere–Duzce rupture zone, the hypocentres indicate a steeply dipping fault to the north. More generally, the locations exhibit a diffuse pattern in a broad region, with clusters near large bends and other geometrical complexities and a possible semi-horizontal detachment structure below 10–13 km (Seeber *et al.* 2000b, in preparation 2003). We note that there are very few hypocentres shallower than 5 km in the vicinity of the large 1999 rupture zones. The nearly complete lack of shallow hypocentres suggests that the top section of the Karadere–Duzce fault is seismically stable and probably consists of highly damaged material that is largely mechanically passive. This is compatible with our structural imaging based on wave propagation effects discussed below, and with observations and inferences made for other tectonically active faults (e.g. Sibson 1983; Marone & Scholz 1988).

The red triangles in Figs 1(a) and (b) mark stations located within a few metres of the surface trace of the rupture. There are clear quantitative and qualitative differences between seismograms recorded at these FZ stations and those observed at neighbouring seismometers located just a few hundred metres from the fault. Waveforms recorded at FZ stations have in general large-amplitude oscillations after the *S* arrivals and clear spectral peaks near 5 Hz. Such characteristics are absent or strongly suppressed at nearby off-fault stations. This is illustrated in Figs 2(a)–(d), where we compare time histories and amplitude spectra of fault-parallel seismograms recorded for several events (Fig. 2e) at neighbouring station pairs located on and off the fault and at T-array stations across the fault. As discussed in Section 1.2, seismic FZ trapped waves are large-amplitude dispersive oscillations that appear in the coda of the direct *S* wave and have particle motion parallel to the FZ structure. Synthetic waveform calculations indicate that trapped waves can produce large-motion amplification in FZ stations for plausible structural properties and propagation distances (Ben-Zion & Aki 1990, Ben-Zion 1998). We thus identify the large-amplitude oscillations after the *S* arrivals that exist in FZ stations and decay rapidly with normal distance from the fault, as FZ trapped waves. The dispersion in these *S*-wave trains is very weak, suggesting that the propagation distance inside the low-velocity FZ material is rather small (e.g. less than 10 km). Weak dispersion also characterizes FZ trapped waves at the Parkfield section of the SAF (Michael & Ben-Zion 1998, 2002) and the Landers rupture zone (Peng *et al.* 2002a,b).

We note that FZ stations have motion amplification not just in the *S*-wave trains but also in the *P* and other portions of the seismograms. Moreover, the differences between on- and off-fault waveforms are generated by nearly all (on- and off-fault) events and they exist not just in fault-parallel seismograms but also in the other components. These characteristics again point to a shallow low-velocity FZ layer. The anomalous behaviour at FZ stations should perhaps be referred to as *fault-zone-related site effects*, rather than the more restrictive term trapped waves. The former term includes in addition to trapped waves proper (i.e. Love-type waves in a vertical layer bounded on one side by a free surface) also basin-type reverberations and other locally amplified phases. While it is important in general to study all these effects, this is not essential to our conclusions. In this work we focus primarily on the high-amplitude long-period wave trains after *S*-wave arrivals in FZ stations and analyse them as trapped waves.

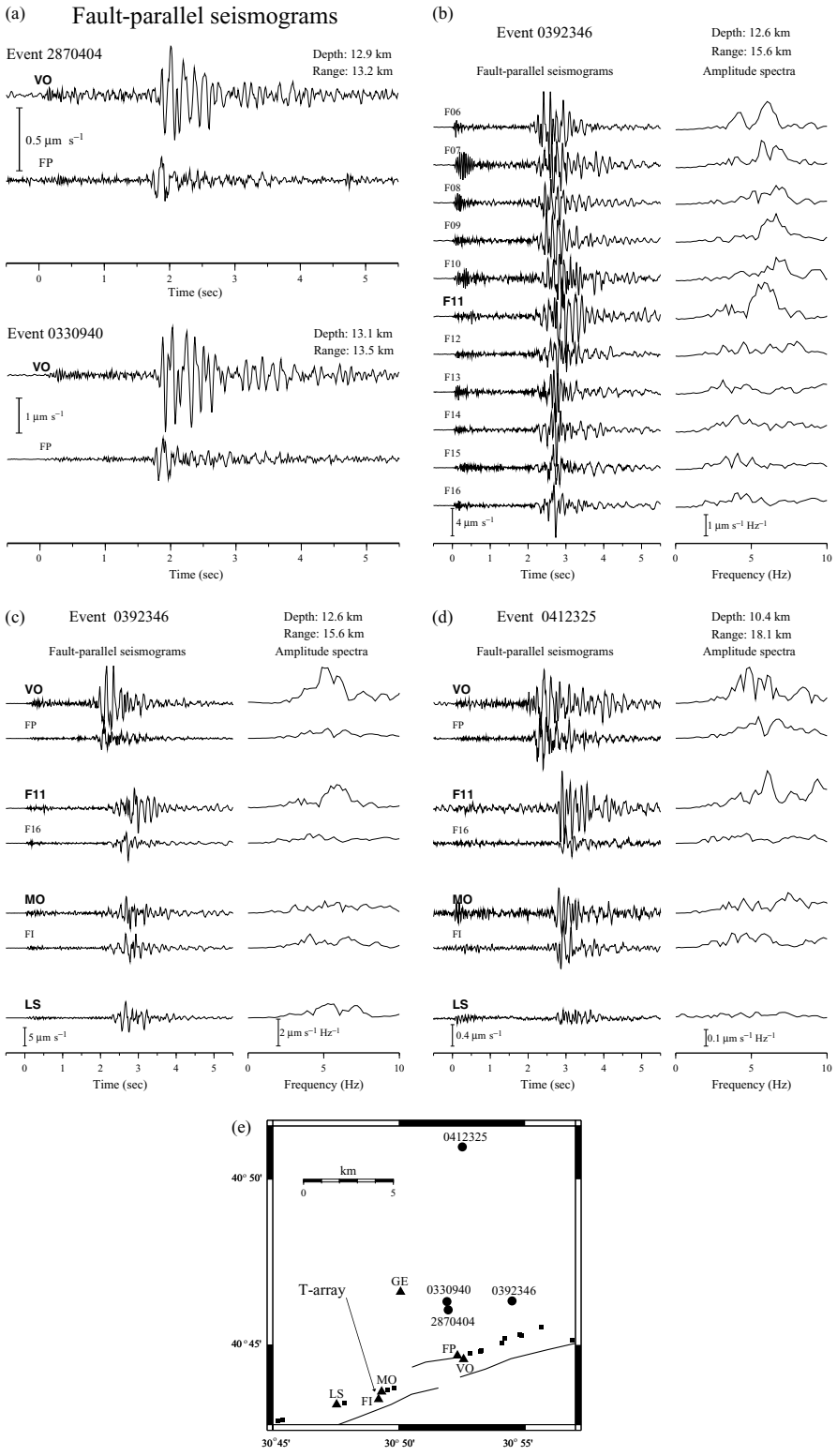

Figure 2. (a) Fault-parallel seismograms recorded at FZ station VO and nearby off-fault station FP for two clustered earthquakes (events 2870404 and 0330940). The event ID numbers consist of a three-digit Julian day, two-digit hour and two-digit minute. Julian days in the range 237–365 are in 1999 and those in the range 001–042 are in 2000. The focal depth and hypocentral distance (range) of the events are given in the top right-hand corner. Station names are marked on the traces with FZ station given in a larger bold font. The event locations are shown in Fig. 2(e). Differences between on and off FZ seismograms of the type shown are produced by the majority of (on and off) fault events. (b) Time histories and amplitude spectra of fault-parallel seismograms recorded at T-array stations across the fault for event 0392346. The amplitude spectra are calculated from the seismograms over a 3 s time window starting from *S* arrivals. The asymmetric motion across the fault is produced by asymmetries in the topography and other local conditions. (c) Time histories and amplitude spectra of fault-parallel seismograms recorded at station pairs on and off the fault for event 0392346. (d) Time histories and amplitude spectra of fault-parallel seismograms recorded at station pairs on and off the fault for event 0412325. (e) A location map of the four events the waveforms of which are shown in (a)–(d).

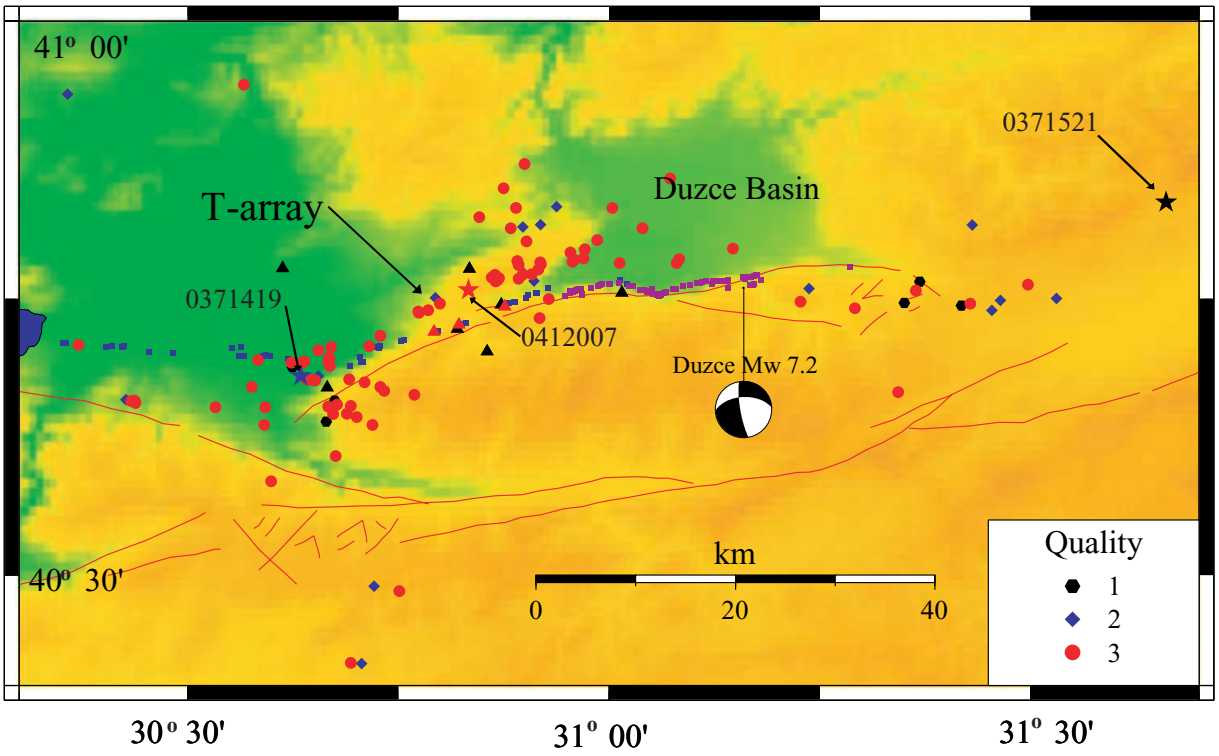

Figure 3. (a) Efficiency of trapped waves generation by 118 events recorded at the T-array during the period 2000 January 30–February 11. Red circles denote 88 events that produce clear trapped waves at all FZ stations. Blue diamonds denote 18 events that generate clear trapped waves at some FZ stations and less developed signals at others. Black hexagons denote seven events that produce trapped waves only at FZ stations F11 and VO. The background colours indicate topography with green being low and orange being high. The waveforms of events marked by stars are shown in Figs 3(b)–(d). Other symbols and notation are the same as in Fig. 1. The broad distribution of events producing trapped waves implies a shallow FZ waveguide. (b) Time histories and amplitude spectra of fault-parallel seismograms recorded at the T-array and other stations for event 0371521. The focal depth and range of the event are marked in the top right-hand corner. The event location is marked with a black star in Fig. 3(a) and is assigned quality 1 for trapped wave generation. (c) Time histories and amplitude spectra of fault-parallel seismograms recorded at the T-array and other stations for event 0371419. The event location is marked with a blue star in Fig. 3(a) and is assigned quality 2 for trapped wave generation. (d) Time histories and amplitude spectra of fault-parallel seismograms recorded at the T-array and other stations for event 0412007. The event location is marked with a red star in Fig. 3(a) and is assigned quality 3 for trapped wave generation. Waveforms produced by this event are modelled in Fig. 11.

The spatial distribution of earthquakes producing trapped waves (and other FZ-related site effects) at surface FZ stations provides first-order information on overall properties of the generating structure. Fig. 3(a) shows the locations of all events (totalling 118) recorded during the ≈2 weeks operation of the T-array by more than half of the array sites along the fault (stations F01–F03 and F11). Five additional five events were not recorded by sufficient FZ stations and are not considered. The locations are coded based on efficiency of trapped waves generation. Red circles denote events that produce clear trapped waves on all FZ stations (quality 3), blue diamonds mark events that generate clear trapped waves on some FZ stations and less developed signals on others (quality 2) and black hexagons mark events that generate trapped waves only at some FZ stations (quality 1). Representative seismograms and spectra associated with each of these categories are given in Figs 3(b)–(d). It is clear from Fig. 3 that virtually all events produce trapped waves at some FZ stations, with over 75 per cent producing clear trapped waves at all FZ stations. Inspection of thousands of waveforms generated by the larger data set of Fig. 1 indicates that the vast majority of the events produce trapped waves (and other FZ-related site effects) at FZ stations. As mentioned in Section 1.2, Igel *et al.* (2002) and Fohrmann *et al.* (2001, 2002) demonstrated with 3-D numerical calculations that events outside a smoothly varying deep FZ layer do not produce trapped waves at surface stations. In contrast, ample trapped waves energy is produced at surface FZ stations by events well outside and below a shallow FZ layer, or well outside and below a severe structural disruption (e.g. offset or near termination) of a deep FZ layer. In the latter set of cases the structures associated with surface records of trapped waves are again shallow. The observed broad spatial distribution of events generating trapped waves in the Karadere–Duzce rupture zone implies that the trapping structure is shallow. This conclusion is confirmed with additional analyses discussed in the following sections.

2.2 Traveltime moveout analysis

To place bounds on the depth extent of the structure generating the high-amplitude long-period *S*-wave trains at FZ stations on the Karadere–Duzce fault, we examine the delay between *S* arrivals and corresponding measures in the trapped waves group for various source locations. Such time differences should increase with propagation distance inside the low-velocity structure and produce a moveout between the body and trapped waves that is related to the velocity structure. This is illustrated in Fig. 4 with synthetic seismograms calculated using the 2-D analytical solution of Ben-Zion & Aki (1990) and Ben-Zion (1998) for antiplane *S* (or acoustic *P*) waves in two quarter-spaces separated by vertical FZ layers. Here we used a simplified structure consisting of a single FZ layer in a

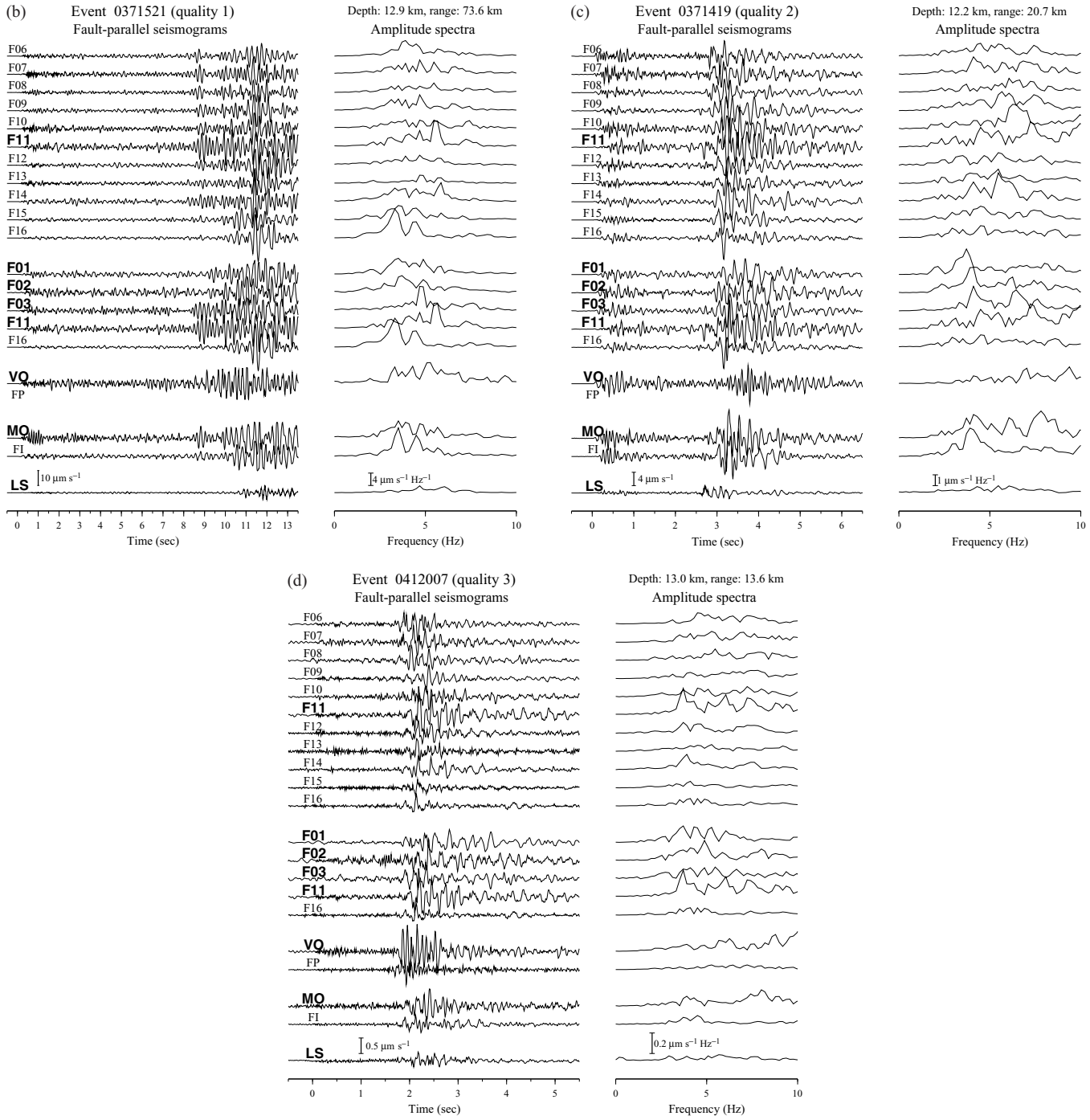

Figure 3. (*Continued*.)

half-space (Fig. 5). The assumed *S*-wave velocity and attenuation coefficient in the half-space are $\beta_H = 3.5$ km s^{-1} and $Q_H = 1000$. The corresponding material properties and width of the FZ layer are $\beta_{FZ} = 2.5$ km s^{-1}, $Q_{FZ} = 50$ and $W = 200$ m. Motion is generated by an *SH* line dislocation with a unit step function in time. The source is located at position x_S, z_S and the receiver is at the centre of the FZ layer. The two solid lines in Fig. 4 with slopes β_H and β_{FZ} mark, respectively, the arrival time of the *S* phase and the end of the trapped waves group, for various values of source depth, representing different propagation distances in the FZ. The end of the trapped waves group is defined as the time for which the amplitude returns to that of the *S* wave. The dashed line in Fig. 4 indicates the centre of the trapped waves group. The time delay between the direct *S* arrival and centre of the trapped waves group is

$$\Delta t = z_S \frac{\beta_H - \beta_{FZ}}{2\beta_H \beta_{FZ}}. \quad (1)$$

Eq. (1) is used below to estimate the depth extent of the low-velocity FZ material in the Karadere–Duzce fault. We note that the value of z_S in our 2-D model represents the total propagation distance inside the FZ region that acts as a waveguide. Since actual propagation paths can include an along-strike component, analysis of observed

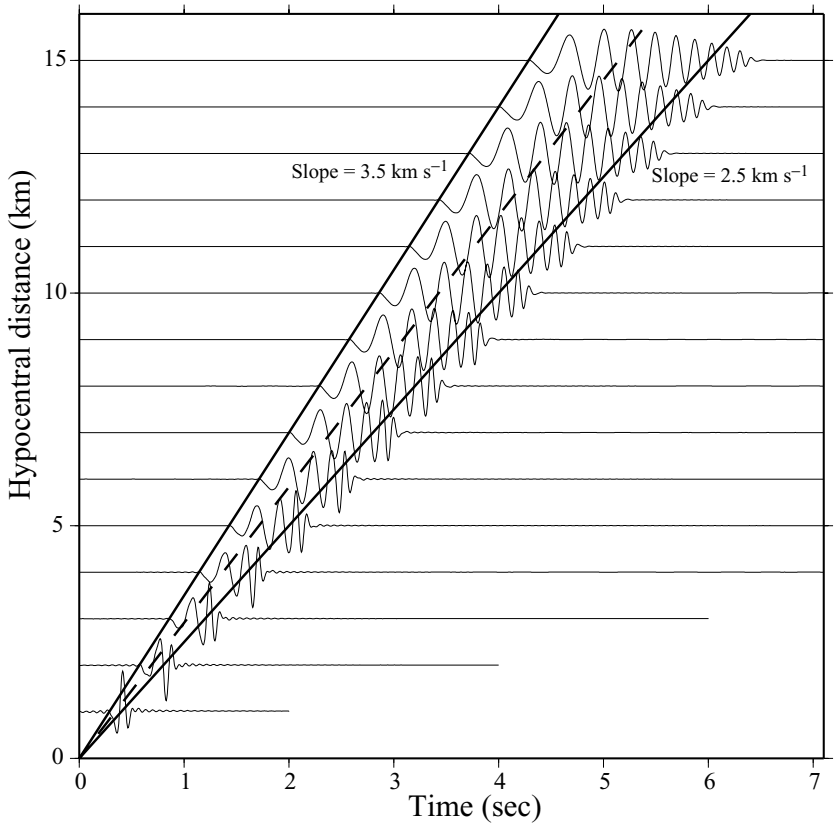

Figure 4. Synthetic seismograms generated using the 2-D analytical solution of Ben-Zion & Aki (1990) and Ben-Zion (1998) with different propagation distances along the FZ. The two solid lines with slopes β_H and β_{FZ} mark, respectively, the arrival time of the *S* phase and the end of the trapped waves group (defined as the time when the amplitude returns to that of the *S* arrival). The dashed line marks the centre of the trapped waves group.

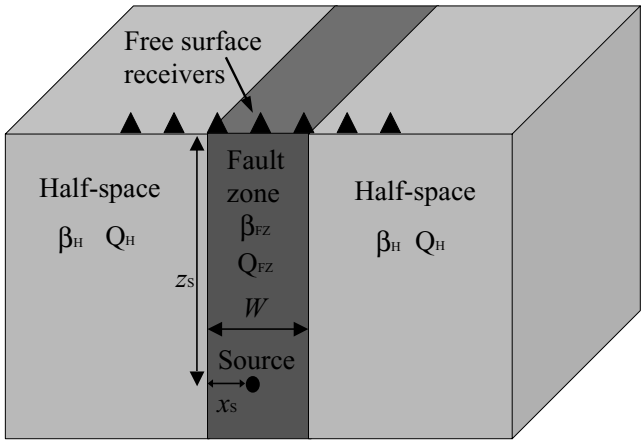

Figure 5. A three-media model for a laterally heterogeneous low-velocity fault-zone structure in a half-space (from Ben-Zion & Aki 1990; Ben-Zion 1998). The source is an *SH* line dislocation with coordinates (x_S, z_S). Width, quality factor and shear wave velocity are marked by W, Q and β, respectively. Subscripts H and FZ denote the half-space and fault-zone layer.

data based on (1) will provide an upper bound to the depth extent of the waveguide. However, for data generated by deep events at a shallow trapping structure, the obtained value will be close to the depth of the structure.

Fig. 6(a) shows fault-parallel seismograms at FZ station VO generated by earthquakes following approximately the downward continuation of the fault. Figs 6(b) and (c) give the event locations (circles) along a cross-section BB′ at the surface and on a vertical plane. We note the lack of shallow events (the minimum earthquake depth in Fig. 6c is approximately 5 km), as discussed in Section 2.1. The ID numbers of the earthquakes are given on the right-hand side of Fig. 6(a) (see the explanation in the caption of Fig. 2a). The seismograms are aligned with the origin time at zero and the thin diagonal line marks the estimated *S* arrival time in each record. The thick diagonal line gives for a reference a shifted *S*-wave moveout for a propagation velocity of 3.3 km s^{-1}. The horizontal bars below and above the seismograms bracket the trapped waves groups and the plus signs show the estimated centres of each group. The latter were measured as mid positions between approximately one oscillation after the *S* arrival and the time when the amplitude reduces back to that of the *S* wave. Since this is somewhat arbitrary, we also measured the times of peak amplitude in each trapped waves group. The results of the moveout analysis discussed next remain essentially the same with either set of measurements.

Fig. 6(d) shows the time delays between *S* arrivals and centres of the trapped waves groups in Fig. 6(a) for the various available hypocentral distances. The data are clustered around an average value of 0.55 s and they do not exhibit a persistent moveout. In fact, the first few data points show a decreasing (rather than an increasing) trend, but this is clearly statistical scatter. It is useful to note in this context the danger of performing a similar analysis with just a few data points (as was done in some previous works with trapped waves). It is always possible to choose a few points that show an increasing (or decreasing) trend over a given range, but this is obviously not representative of a real moveout. The lack of moveout in Fig. 6(a) implies that the propagation distance inside

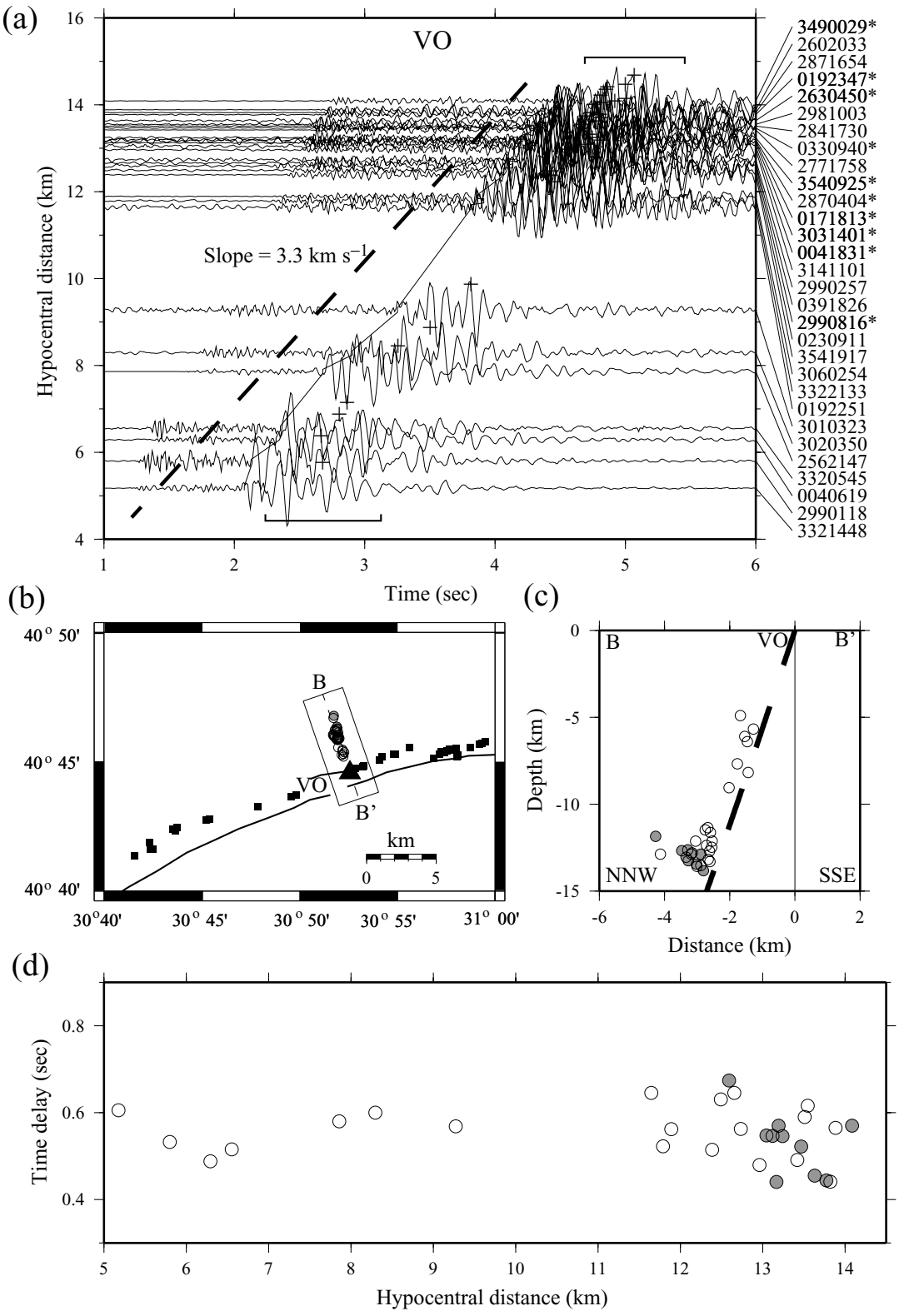

Figure 6. (a) Fault-parallel seismograms at station VO for events at cross-section BB′ following approximately the downward continuation of the fault. The thin diagonal line marks the estimated *S* arrival time in each record. The thick dashed line gives a shifted *S*-wave moveout for a propagation velocity of 3.3 km s^{-1}. The horizontal bars below and above the seismograms denote time windows of FZ trapped waves. The plus sign on top of each seismogram marks the centre of the trapped waves group. The ID numbers of the earthquakes are given on the right-hand side. The waveforms of the 10 events for which the ID numbers are marked with asterisks are modelled in Fig. 10. (b) A location map of the events producing the seismograms shown in (a). Grey circles mark the locations of the 10 events for which the waveforms are modelled in Fig. 10. (c) Hypocentres projected from the box in (b) on a vertical plane along the cross-section BB′. (d) Time differences between *S* arrivals and centres of trapped waves groups for different hypocentral distances. The lack of a systematic increase with hypocentral distance implies an approximately constant propagation length in the FZ waveguide.

the low-velocity FZ structure in our study area is less than 5 km. Synthetic waveform modelling of FZ waves observed at station VO and across the T-array, discussed in Section 2.3, indicates that the average (or effective) *S*-wave velocities of the host rock and FZ material are approximately 3.2 and 1.5 km s^{-1}, respectively. Using these values in (1) together with $\Delta t = 0.55$ s gives a waveguide depth of approximately 3 km. Similar values for the depth extent of the trapping structure are indicated by the waveform modelling of Section 2.3.

Figs 7(a)–(d) and 8(a)–(d) give results analogous to those of Figs 6(a)–(d) for seismic records at station VO generated by events along two other cross-sections, one (CC′) normal and the other (DD′) parallel to the surface trace of the fault. The events along CC′ are deeper than approximately 5 km as in profile BB′, while those along DD′ are deeper than approximately 10 km. In contrast with the events in profile BB′ of Fig. 6, the hypocentral distances of the events in Figs 7 and 8 are larger than their corresponding depth values since profiles CC′ and DD′ are not along the fault. For easier visual comparison of the trapped waves groups generated by the different events, the seismograms in Figs 7 and 8 are aligned with the *S* arrivals. As before, the time delays between the *S* arrivals and centres of the trapped waves groups cluster around 0.55 s without any persistent moveout. Figs 9(a)–(d) provide similar results for seismic records at station F11 in the centre of the T-array, produced by events along the cross-section DD′. Again, there is no persistent moveout between the *S* and trapped waves. The average delay time is somewhat larger (approximately 0.6 s) than that observed at station VO. The results of Figs 6–9 demonstrate clearly that the depth extent of the low-velocity structure generating the large-amplitude long-period wave trains in FZ stations is less than 5 km. This is compatible with synthetic waveform fits of FZ waveforms discussed in the next section.

2.3 Synthetic waveform modelling of FZ waves

To substantiate and augment the results based on traveltime analysis, we perform synthetic modelling of FZ waveforms using the 2-D analytical solution of Ben-Zion & Aki (1990) and Ben-Zion (1998) for scalar elastodynamic waves in a plane-parallel layered FZ structure. The solution can be used to model portions in both *P* and *S* waveforms containing body waves, head waves, reflections from the free surface and FZ walls, and trapped waves. The model allows for an arbitrary number of vertical layers, a large propagation distance, attenuation effects, variable source location inside and outside the FZ, and a variable receiver depth below the free surface. In the present application, we find that candidate trapped waves recorded on the Karadere–Duzce rupture zone can be modelled well with a single FZ layer in a half-space (Fig. 5) and that simplified structure is used below.

An apparent limitation of the solution is that it does not account for 3-D variations of geometrical and material properties. In practice, however, this is not a severe restriction for modelling FZ *trapped waves* since those are essentially 2-D phases that average (over the generated wavelengths) small-scale or gradual internal variations of FZ properties. Indeed, Igel *et al.* (1997, 2002) and Jahnke *et al.* (2002) showed with extensive 3-D finite-difference calculations that FZ trapped waves are not sensitive to various plausible 3-D variations of FZ structure with correlation length smaller than the overall FZ width. These include gradual variations of properties across the fault, vertical velocity gradients, internal scatterers and other small-scale heterogeneities. On the other hand, material or geometrical heterogeneities (e.g. structural offsets) of size larger than the FZ width destroy the ability of the FZ to act as a waveguide; trapped waves energy arriving at such large-scale heterogeneities is diffused in the bulk. The 2-D solution can thus be used to derive from observed trapped waves effective waveguide properties of FZ segments over which the waves propagate. (We return to this issue in the discussion section.) As shown below, the solution provides good fits to trapped waves observed at FZ stations on the Karadere–Duzce fault.

While FZ guided waves are not sensitive to small-scale 3-D variations, a systematic 2-D parameter space study indicates (Ben-Zion 1998; Michael & Ben-Zion 1998) that they are *highly* sensitive to variations of the average 2-D properties and source–receiver–fault configuration. These include the overall velocity contrast within and across the fault, the attenuation coefficient of the FZ material, the ratio of the propagation distance along the fault divided by the FZ width and source–receiver positions with respect to the fault and free surface. Moreover, the 2-D analysis indicates that there are significant non-orthogonal trade-offs between the overall 2-D fault-zone properties (Ben-Zion 1998). Thus the proper resolution of the effective or average 2-D properties of FZ layers from observed trapped waves is a very challenging task. In the simple model of Fig. 5 there are four sensitive material properties (wave velocities and attenuation coefficients of the FZ and host rock) and four sensitive geometrical parameters (FZ width, propagation distance inside the FZ layer, source position within the fault and receiver distance from the fault). Fixing the attenuation coefficient of the host rock at 1000 and receiver positions based on the network geometry, we are left with six sensitive parameters. This can be further reduced by using the ratio of propagation distance in the FZ divided by the FZ width and velocity contrast across the fault, rather than the associated four parameters independently. Since the parameters are non-orthogonal, however, the dimensionality of the remaining parameter space is larger than four. To provide a systematic objective treatment of this multidimensional parameter space, we model observed FZ waveforms with a genetic inversion algorithm (GIA) that employs the 2-D analytical solution as a forward kernel (Michael & Ben-Zion 1998, 2002).

Another simplification of the 2-D solution is the assumed line dislocation source (of infinite extent in and out of the plane of Fig. 5) parallel to the material interfaces and the free surface. The limitations associated with the assumed source can be reduced by deconvolving the synthetic seismograms with $1/t^{1/2}$ (e.g. Vidale *et al.* 1985; Crase *et al.* 1990; Igel *et al.* 2002) and modelling only fault-parallel seismograms. Igel *et al.* (2002) demonstrated with 2-D and 3-D calculations that the above deconvolution provides, for the problem at hand, an accurate conversion of 2-D seismograms generated by an *SH* line source to corresponding 3-D seismograms generated by a point source. Our modelling procedure includes such a 2-D–3-D transformation and is applied only to fault-parallel seismograms. The solution can probably also be used to model vertical seismograms (having particle motion parallel to the FZ interfaces) but this is not done here. We also note that dislocation in the FZ layer may not be the best source representation in this problem. However, the exact nature of the source does not have strong effects on FZ trapped waves since ideally they give the (free or eigen) resonance response of the FZ structure after transient effects associated with the source decay (Ben-Zion & Aki 1990). Varying the horizontal source position inside the FZ layer provides an effective way of changing the resulting interference patterns (which may be produced by sources outside and below the FZ layer).

Fig. 10(a) shows synthetic (dark lines) waveform fits to 10 displacement seismograms (light lines) at FZ station VO generated by

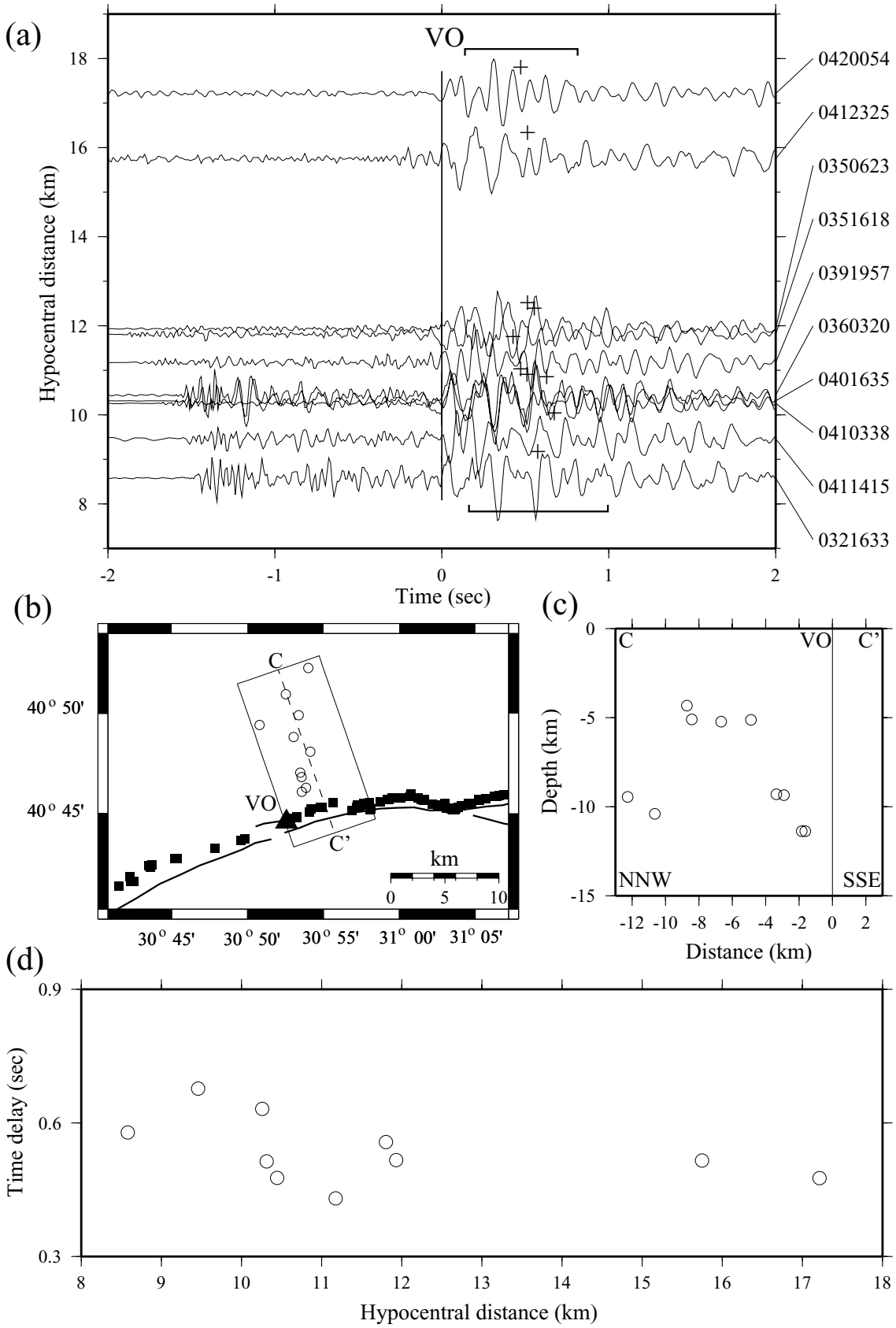

Figure 7. (a) Fault-parallel seismograms at station VO for events at cross-section CC′ perpendicular to the fault strike. Other symbols and notation are the same as in Fig. 6(a). (b) A location map of the events producing the waveforms shown in (a). (c) Hypocentres projected from the box in (b) on a vertical plane along the cross-section CC′. (d) Time differences between *S* arrivals and centres of trapped waves groups for different hypocentral distances. The lack of a systematic increase with hypocentral distance implies an approximately constant propagation length in the FZ waveguide.

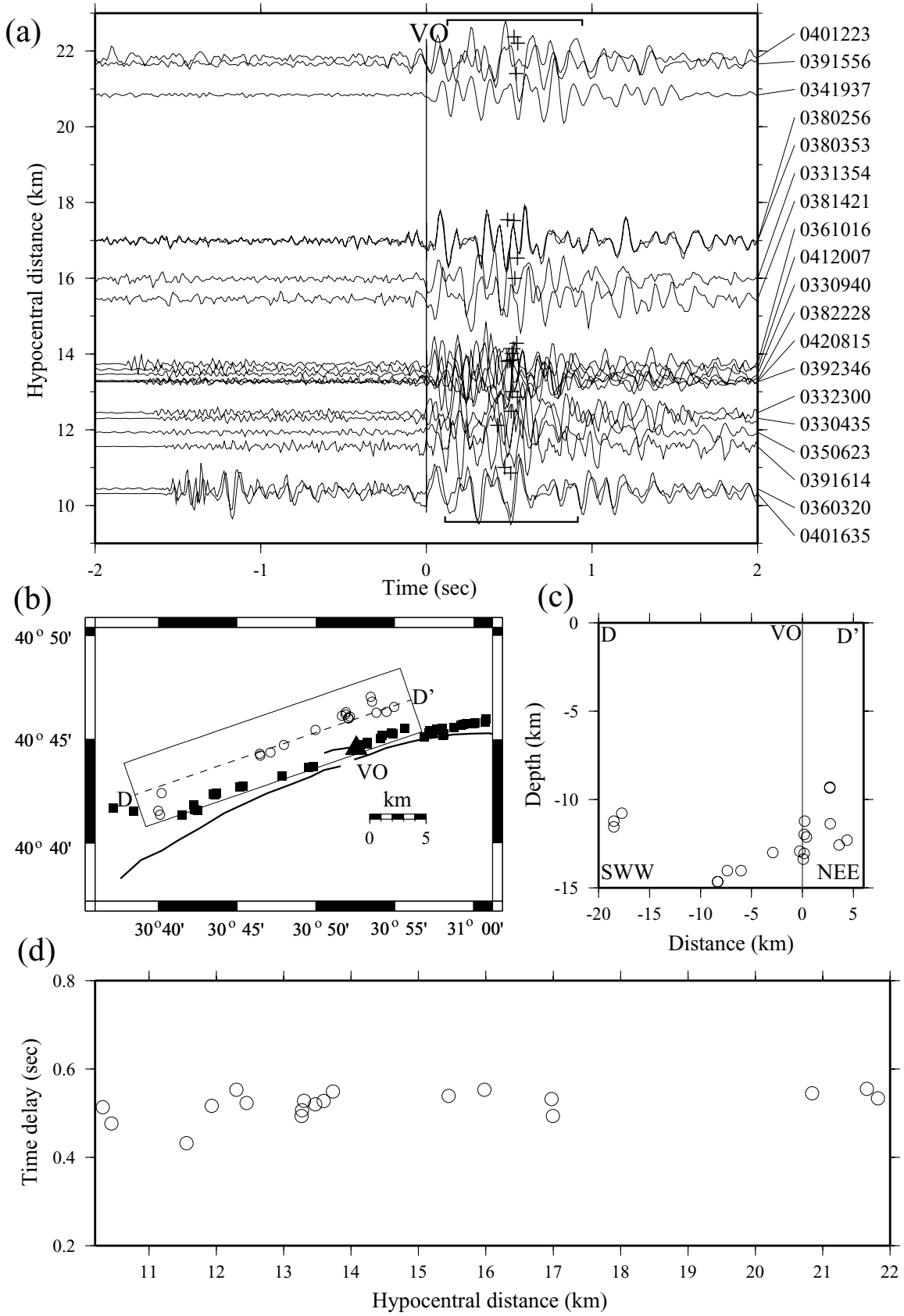

Figure 8. (a) Fault-parallel seismograms at station VO for events at cross-section DD′ parallel to the fault strike. Other symbols and notation are the same as in Fig. 6(a). (b) A location map of the events the waveforms of which are shown in (a). (c) Hypocentres projected from the box in (b) on a vertical plane along the cross-section DD′. (d) Time differences between *S* arrivals and centres of trapped waves groups for different hypocentral distances. The lack of a systematic increase with hypocentral distance implies an approximately constant propagation length in the FZ waveguide.

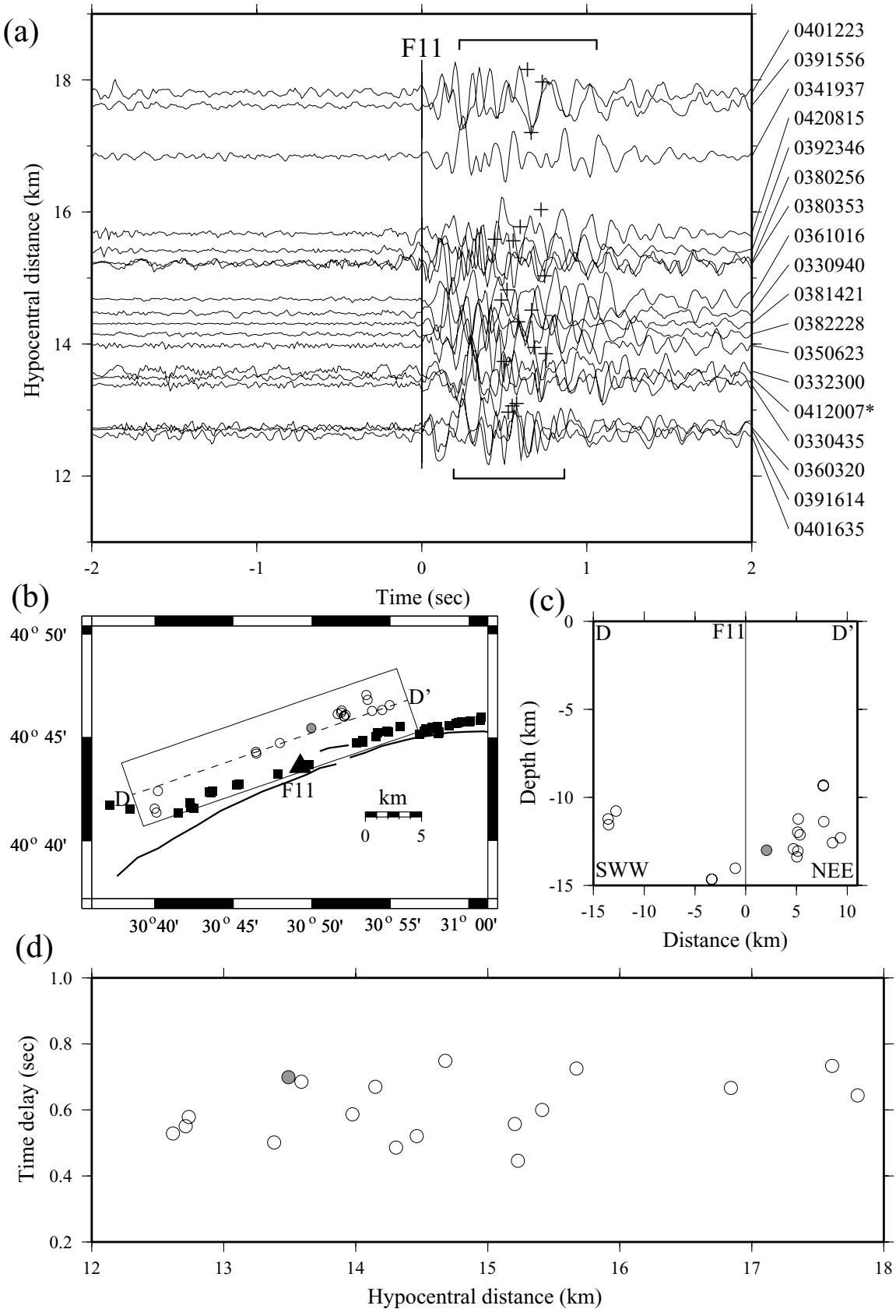

Figure 9. Fault-parallel seismograms at station F11 for events at cross-section DD′ parallel to the fault strike. Other symbols and notation are the same as in Fig. 6(a). (b) A location map of the events producing the seismograms shown in (a). (c) Hypocentres projected from the box in (b) along the cross-section DD′. (d) Time differences between *S* arrivals and centres of trapped waves groups for different hypocentral distances. The waveforms of event 0412007 marked with an asterisk in (a) and grey circles in (b)–(d) are modelled in Fig. 11.

the cluster of events marked with grey circles in Fig. 6. As discussed above, the waveform modelling is done with the GIA of Michael & Ben-Zion (1998) based on the 2-D solution of Ben-Zion & Aki (1990) and Ben-Zion (1998) for the model shown in Fig. 5. Before inversion, the mean and instrument response are removed from observed seismograms using standard SAC routines. Also, following the foregoing discussion the observed data are rotated to the fault-parallel direction (70°) and convolved with $1/t^{1/2}$. The GIA maximizes the correlation between sets of observed and synthetic waveforms (10 each in this case), while performing a systematic exploration of a large parameter space. This is accomplished by calculating fitness values associated with different sets of model parameters and migrating in the parameter space (i.e. evolving) overall in the direction of larger fitness values. The fitness is defined as $(1 + C)/2$, where C is the cross-correlation coefficient between the observed and synthetic waveforms. When C varies over the range -1 (perfect anticorrelation) to 1 (perfect correlation), the fitness value changes from 0 to 1.

The synthetic waveform fits of Fig. 10(a) were produced during 10 000 inversion iterations (testing 10 000 sets of model parameters). Fig. 10(b) shows fitness values (dots) calculated by the GIA for the final 2000 iterations. The model parameters associated with the highest fitness values were used to produce the simultaneous waveform fits of Fig. 10(a). The best-fitting parameters (solid circles) are $\beta_{FZ} = 1.6$ km s^{-1}, $Q_{FZ} = 10$, $W = 60$ m, $x_S/W = 0.18$, $z_S = 4.6$ km, $\beta_H = 3.2$ km s^{-1} and $Q_H = 1000$. The curves in Fig. 10(b) give probability density functions for the various model parameters, calculated by summing the fitness values of the final 2000 inversion iterations and normalizing the results to have unit sums. The obtained functions are similar to the marginal probability densities (Tarantola 1987) that quantify the information contained in single model parameters by collapsing the joint probability of a multidimensional inverse problem (if such is available) to the corresponding parameter axis. The peaks in the probability density functions provide another possible set of preferred model parameters. The preferred probability value for the FZ depth is 3.6 km. We recall that our 2-D calculations map the entire propagation distance inside the waveguide to the depth parameter. The inversion results thus give an upper bound of approximately 4 km for the depth extent of the trapping structure below the surface trace of the Karadere–Duzce fault. This is similar to the estimate made in Section 2.1 based on traveltime analysis. The preferred inversion value of β_H is approximately 3.2 km s^{-1}, in general agreement with the 3.3 km s^{-1} line of Fig. 6 that approximates the observed moveout of the *S* phase.

Fig. 11(a) shows synthetic waveform fits of the GIA to nine fault-parallel seismograms recorded at T-array stations and nearby FZ stations MO and F03 (Fig. 1). The seismograms are generated by the event marked with a grey circle in Fig. 9. The waveform fits were produced again by 10 000 inversion iterations and the fitness values associated with the final 2000 iterations are given in Fig. 11(b). The synthetic waveform fits are somewhat less good than in Fig. 10, probably because of the steep topography of the T-array stations normal to the fault (not accounted for in the calculations). Here the preferred model value for the FZ width is approximately 90 m. The other preferred values are similar to those of Fig. 10.

The relatively flat regions in Figs 10(b) and 11(b) with relatively high fitness values are a manifestation of the strong trade-offs between the parameters that govern FZ trapped waves. Moreover, it is possible to obtain good fits to the observed waveforms with parameter values well outside the used ranges. We can, for example, fit the data with considerably larger FZ propagation distances (e.g. 10 km) if we change other parameters (various combinations of FZ width, velocity and attenuation coefficient) in an appropriate compensatory manner. Ben-Zion (1998) illustrates various trade-offs in this problem with corresponding sets of model calculations. The strong trade-offs may explain why Li & Leary (1990) and Li *et al.* (1994, 1998) were able to fit trapped waves at Parkfield and the 1992 Landers rupture with models of FZ layers that span the seismogenic zones, while the analyses of Michael & Ben-Zion (1998), Korneev *et al.* (2002) and Peng *et al.* (2002) point to considerably shallower trapping structures. The strong trade-offs between model parameters governing trapped waves highlight the need to use large data sets and perform simultaneously different types of analysis that can provide independent constraints and reduce together the allowed parameter space volume.

3 DISCUSSION

We analyse waveform and traveltime properties of a large seismic data set recorded in the 6 months after the 1999 $M_w = 7.4$ Izmit earthquake by a local PASSCAL network on the Karadere–Duzce branch of the NAF. Seismograms observed at sites located within tens of metres from the surface expression of the rupture zone have large-motion amplification with respect to nearby off-fault stations. Following the direct *S* arrival in FZ seismograms, there are large-amplitude long-period oscillations that can be interpreted as trapped waves propagating in a layer of damaged FZ rock. The large-amplitude oscillations in FZ waveforms are generated by the vast majority of events (Figs 2 , 3 and 6–9), most of which are well outside the Karadere–Duzce rupture zone. The anomalous features at FZ stations may be referred to in general as FZ-related site effects. The latter also include, along with trapped waves, resonance effects in sedimentary covers, basins and other topographic features that are often associated with fault structures near the surface. In this paper we ignore these additional wave propagation effects and analyse shear wave portions of FZ seismograms solely in terms of direct *S* and FZ trapped waves. A fuller treatment of the set of features contributing to the FZ-related site effects requires 3-D calculations that are beyond the scope of the present work and not essential for our conclusions. The 2-D analytical solution of Ben-Zion & Aki (1990) and Ben-Zion (1998) for a uniform seismic waveguide in a half-space (Fig. 5) provides guidelines for traveltime analysis and is used, together with the genetic inversion algorithm of Michael & Ben-Zion (1998), to fit observed FZ shear waveforms. The traveltime and waveform analyses indicate (Figs 6–11) that the depth of the structure along the Karadere–Duzce fault producing the large-amplitude long-period oscillations at FZ stations is approximately 3–4 km. A shallow trapping structure is also implied by the broad spatial distribution of events generating the large-amplitude oscillatory wave trains at FZ stations (Fohrmann *et al.* 2001, 2002; Igel *et al.* 2002).

Fig. 12 illustrates the qualitative difference between the shallow trapping FZ structure supported by the analysis of the present work and the deep coherent FZ layers that were assumed in most previous modelling (e.g. Li *et al.* 1994, 2000) of trapped waves. Haberland *et al.* (2001) recently inferred from analyses of trapped waves and other seismic data on the existence of a shallow damaged FZ layer, extending to a depth of only approximately 1 km, in the Arava segment of the Dead Sea Transform. Rovelli *et al.* (2002) concluded on a similar depth extent of a damaged FZ layer in a dormant fault in Nocera Umbra in Italy. As mentioned before, relatively shallow

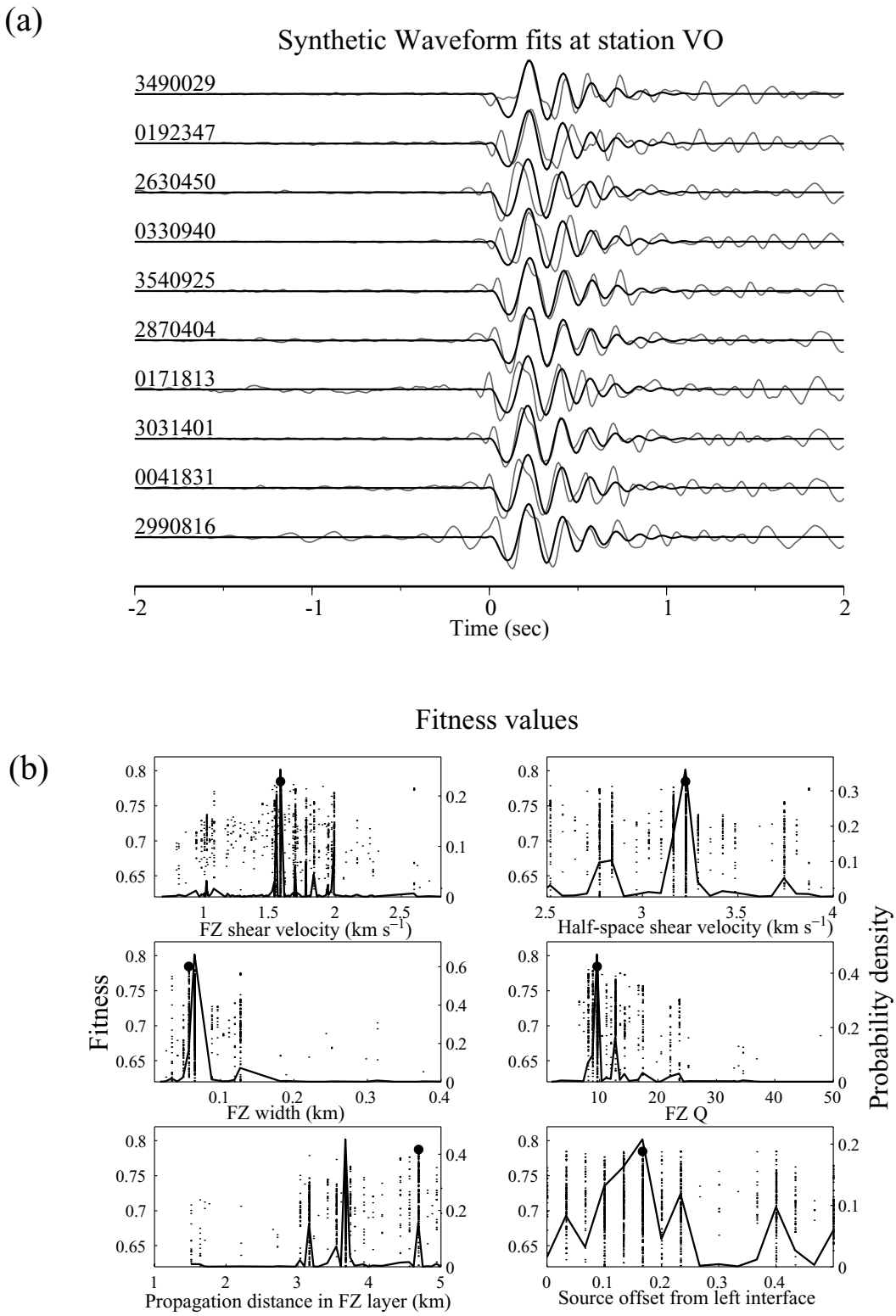

Figure 10. (a) Synthetic (dark lines) waveform fits of 10 fault-parallel displacement seismograms (light lines) at station VO generated by the cluster of events (numbers on traces) marked in Fig. 6. (b) Fitness values (dots) associated with different FZ parameters tested by the genetic inversion algorithm. The model parameters associated with the highest fitness values (solid circles) were used to generate the synthetic waveforms in (a). The curves give probability density functions for the various model parameters.

trapping structures are also indicated by the analyses of Michael & Ben-Zion (1998, 2002) and Korneev *et al.* (2002) at the Parkfield segment of the SAF, and Peng *et al.* (2002a,b) at the rupture zone of the 1992 Landers earthquake. It is likely that shallow trapping FZ structures of the type shown in Fig. 12(a) are the rule rather than the exception. The shallow trapping layers may correspond to the top part of a 'flower' structure or may exist as isolated regions of damaged FZ rock. At present, there is no convincing evidence for

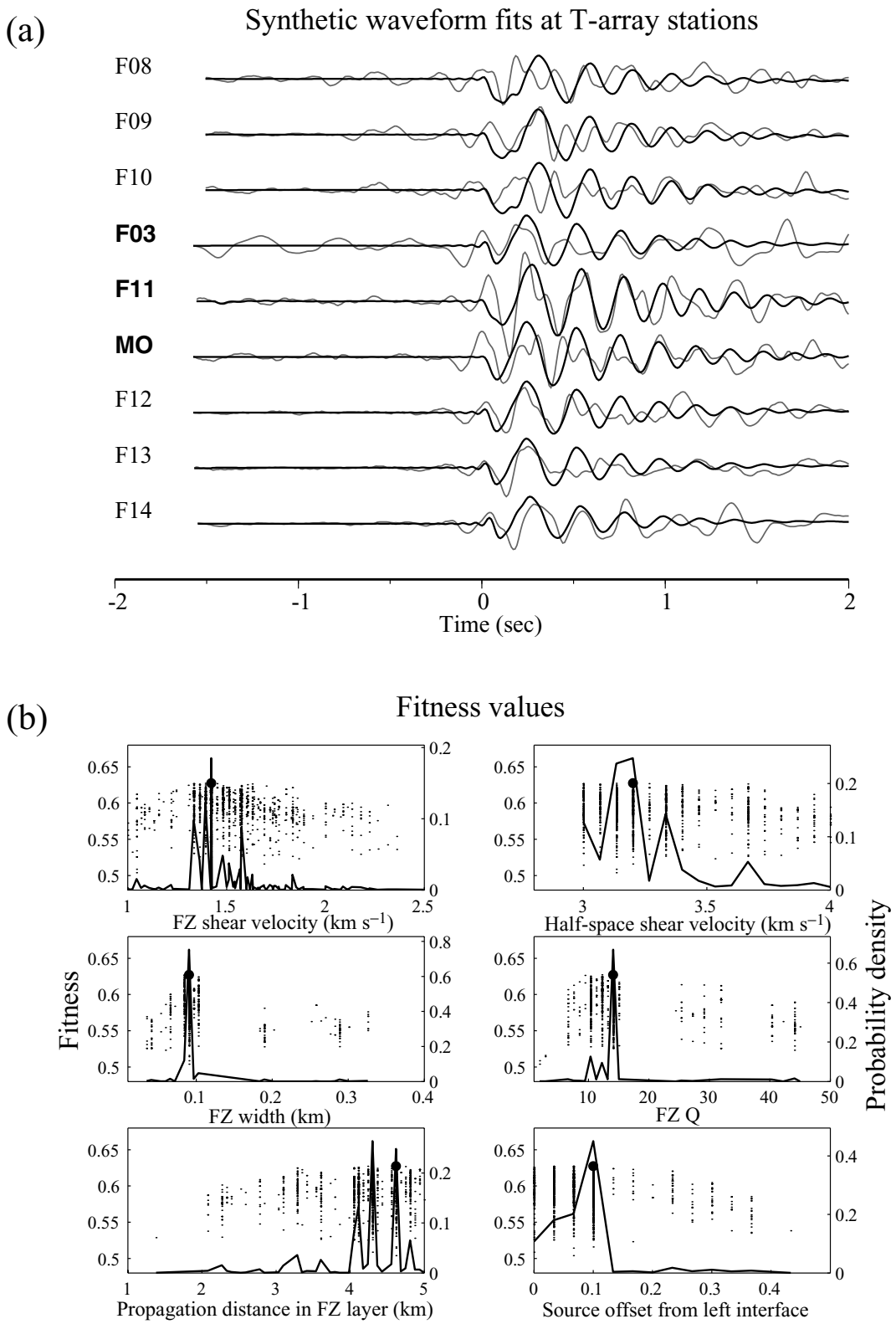

Figure 11. (a) Synthetic (dark lines) waveform fits of displacement seismograms (light lines) recorded at T-array stations and nearby FZ stations MO and F03 for event 0412007. (b) Fitness values (dots) associated with different FZ parameters tested by the genetic inversion algorithm. The model parameters associated with the highest fitness values (solid circles) were used to generate the synthetic waveforms in (a). The curves show probability densities for the various model parameters.

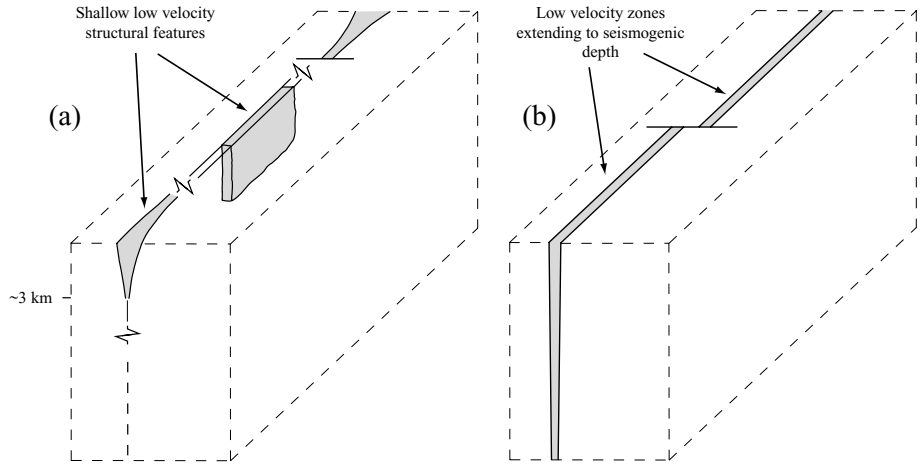

Figure 12. (a) A conceptual fault-zone model supported by the results of the present work. (b) A conceptual fault-zone model used in a previous observational analysis of trapped waves.

the existence and properties of deep coherent FZ layers of the type shown in Fig. 12(b). We note that the significance of the shallow trapping structures of Fig. 12(a) for seismic shaking hazard is considerably larger than that associated with the deep coherent FZ layer of Fig. 12(b). This is because the former class can generate motion amplification from a much broader spatial distribution of events, and from large ruptures on the main fault (Seeber *et al.* 2000a).

Given the 3-D nature of the low-velocity damage zones in Fig. 12(a), one may question the validity of modelling trapped waves in such structures with 2-D calculations. However, if the FZ width is much smaller than the length and depth dimensions of the damage zone, and much larger than correlation lengths of internal geometrical and material heterogeneities, the correct dimensionality for guided waves is 2-D. As discussed in Section 2.3, trapped waves will not exist in FZ regions that are too heterogeneous to be approximated locally as 2-D structures (Igel *et al.* 1997). Conversely, when trapped waves exist they do not resolve internal 3-D variations of the FZ segments over which they propagate (Igel *et al.* 2002; Jahnke *et al.* 2002). The validity of using the 2-D solution of Ben-Zion & Aki (1990) and Ben-Zion (1998) for modelling observed trapped waves is indicated by its ability to provide good waveform fits to the data (Figs 10a and 11a). The same solution also produces good fits to observed guided waves at the Parkfield segment of the SAF (Ben-Zion & Malin 1991; Michael & Ben-Zion 1998) and areas of the 1992 Joshua-Tree (Hough *et al.* 1994) and Landers (Peng *et al.* 2002) earthquakes (see also Kuwahara & Ito 2000; Haberland *et al.* 2001; Nishigami *et al.* 2001). Modelling properly other portions of seismograms, rather than just those containing guided waves, or additional FZ-related site effects would probably require 3-D calculations.

It is important to continue efforts to resolve properties of fault zones below the shallow trapping structures represented by Fig. 12(a). Our study does not provide direct information on the deep structure of the Karadere–Duzce rupture zone, beyond not supporting the existence of a deep contiguous or smoothly varying damage zone of the type shown in Fig. 12(b). It is highly likely that the width of the rupture zone at seismogenic depths (e.g. below 5 km) is considerably less than the approximately 100 m width that characterizes the shallow trapping structure and rupture zone at the surface. Chester *et al.* (1993), Chester & Chester (1998), Schulz & Evans (2000), Neal *et al.* (2000) and Evans *et al.* (2000) provided detailed information on the internal structure of several exhumed fault zones in California, including the San Gabriel, Punchbowl and Kern Canyon faults and various small faults in the Sierra Nevada. In all those cases they documented extremely narrow core layers (2–3 mm thick in small faults with 10 cm of slip in the Sierra Nevada; 10–20 cm thick in the Punchbowl fault with 40 km of slip) that accommodated most of the deformation sustained by the faults. Ben-Zion & Sammis (2003) summarized multidisciplinary multiresolution evidence from field observations, laboratory data and theory on the geometrical and mechanical character of fault zones. The results indicate consistently that fault and rupture zones tend to evolve overall with cumulative slip towards narrow tabular and planar structures. A positive feedback between strain weakening rheology and localization leads to progressive regularization and narrowing of slip zones in active faults. It is probably safe to assume that current surface imaging techniques cannot resolve accurately the deep properties of the active mechanical components (i.e. rupture zones) of faults. Clarifying the properties of the key mechanical structure of faults at seismogenic depths will require multidisciplinary research combining field studies of exhumed faults, laboratory experiments of material properties, highly accurate hypocentre locations, measurements in (preferably deep) boreholes and mines, and innovative joint analyses of different seismic and other indirect geophysical signals.

ACKNOWLEDGMENTS

We thank PASSCAL for providing the equipment and technical support for the experiment, Turkish Airlines (THY) for facilitating the fieldwork by allowing free transportation for the equipment, and the many local residents near the deployment sites for their remarkable cooperation and hospitality. The manuscript benefited from useful comments by Heiner Igel, Michael Korn and Tuncay Taymaz. The studies were supported by the National Science Foundation (grants EAR0003401 to USC and EAR0087798 to LDEO).

REFERENCES

Armijo, R., Meyer, B., Barka, A., De Chabaler, D. & Hubert-Ferrari, A., 1999a. The 1999 Izmit earthquake rupture and the tectonic evolution of the Sea of Marmara, *EOS, Trans. Am. geophys. Un.,* **80,** F664.

Armijo, R., Meyer, B., Hubert, A. & Barka, A., 1999b. Westward propagation of the North Anatolian fault into the northern Aegean: timing and kinematics., *Geology,* **27,** 267–270.

Barka, A.A., 1996. Slip distribution along the North Anatolian Fault associated with large earthquakes of the period 1939 to 1967, *Bull. seism. Soc. Am.,* **86,** 1238–1254.

Barka, A.A. & Kadinsky C., 1988. Strike-slip fault geometry in Turkey and its influence on earthquake activity, *Tectonophysics,* **7,** 663–684.

Barka, A., Kazaci, O., Akyuz S. & Altunel, E., (eds) 2000. *The 1999 Izmit and Duzce Earthquakes: Preliminary Results*, Istanbul technical university, Istanbul.

Ben-Zion, Y., 1998. Properties of seismic fault zone waves and their utility for imaging low velocity structures, *J. geophys. Res.,* **103,** 12 567–12 585.

Ben-Zion, Y. & Aki, K., 1990. Seismic radiation from an *SH* line source in a laterally heterogeneous planar fault zone, *Bull. seism. Soc. Am.,* **80,** 971–994.

Ben-Zion, Y. & Malin, P., 1991. San Andreas fault zone head waves near Parkfield, California, *Science,* **251,** 1592–1594.

Ben-Zion, Y. & Sammis, C.G., 2003. Characterization of Fault Zones, *Pure appl. Geophys.,* **160,** 677–715.

Ben-Zion, Y., Katz, S. & Leary, P., 1992. Joint inversion of fault zone head waves and direct *P* arrivals for crustal structure near major faults, *J. geophys. Res.,* **97,** 1943–1951.

Chester, F.M. & Chester, J.S., 1998. Ultracataclasite structure and friction processes of the Punchbowl fault, San Andreas system, California, *Tectonophysics,* **295,** 199–221.

Chester, F.M., Evans, J.P. & Biegel, R.L., 1993. Internal structure and weakening mechanisms of the San Andreas fault, *J. geophys. Res.,* **98,** 771–786.

Cormier, V.F. & Spudich, P., 1984. Amplification of ground motion and waveform complexities in fault zones: examples from the San Andreas and the Calaveras faults, *Geophys. J. R. astr. Soc.,* **79,** 135–152.

Crase, E., Pica, A., Noble, M., McDonald, J. & Tarantola, A., 1990. Robust elastic nonlinear inversion: application to real data, *Geophysics,* **55,** 527–538.

Evans, J.P., Shipton, Z.K., Pachell, M.A., Lim, S.J. & Robeson, K., 2000. The structure and composition of exhumed faults, and their implication for seismic processes, in *Proc. 3rd Conf. on Tecto. Problems of the San Andreas System*, Stanford University.

Fohrmann, M., Jahnke, G., Igel, H. & Ben-Zion, Y., 2001. Guided waves generated by sources outside a low velocity fault zone layer, *EOS, Trans. Am. geophys. Un.,* **82,** F886.

Fohrmann, M., Jahnke, G., Igel, H. & Ben-Zion, Y., 2002. Guided waves from sources outside faults: an indication for shallow fault zone structure?, *Pure appl. Geophys.,* submitted

Fukao, Y., Hori, S. & Ukawa, M., 1983. A seismological constraint on the depth of basalt–eclogite transition in a subducting oceanic crust, *Nature,* **303,** 413–415.

Haberland, C. *et al.*, 2001. Observation of guided waves at the Wadi Arava Fault, Jordan, *EOS, Trans. Am. geophys. Un.,* **82,** F885.

Hori, S., Inoue, H., Fukao Y. & Ukawa, M., 1985. Seismic detection of the untransformed 'basaltic' oceanic crust subducting into the mantle, *Geophys. J. R. astr. Soc.,* **83,** 169–197.

Hough, S.E., Ben-Zion, Y. & Leary, P., 1994. Fault-zone waves observed at the southern Joshua Tree earthquake rupture zone, *Bull. seism. Soc. Am.,* **84,** 761–767.

Huang, B.-S., Teng, T.-L. & Yeh, Y.T., 1995. Numerical modeling of fault-zone trapped waves: acoustic case, *Bull. seism. Soc. Am.,* **85,** 1711–1717.

Igel, H., Ben-Zion, Y. & Leary, P., 1997. Simulation of *SH* and *P–SV* wave propagation in fault zones, *Geophys. J. Int.* **128,** 533–546.

Igel, H., Jahnke, G. & Ben-Zion, Y., 2002. Numerical simulation of fault zone guided waves: accuracy and 3-D effects, *Pure appl. Geophys.,* **159,** 2067–2083.

Jackson, J. & McKenzie, D.P., 1988. The relationship between plate motion and seismic moment tensors, and the rates of active deformation in the Mediterranean and Middle East, *Geophys J.,* **93,** 45–73.

Jahnke, G., Igel, H. & Ben-Zion, Y., 2002. Three-dimensional calculations of fault zone guided wave in various irregular structures, *Geophys. J. Int.,* **151,** 416–426.

Klein, W., 1978. Hypocenter location program HYPOINVERSE, USGS Open File Report 78–694.

Korneev, V.A., Nadeau, R.M. & McEvilly, T.V., 2002. Seismological studies at Parkfield IX: fault-zone imaging using guided wave attenuation, *Bull. seism. Soc. Am.*, submitted

Kuwahara, Y. & Ito, H., 2000. Deep structure of the Nojima fault by trapped wave analysis, USGS, Open-file report 00-129, 283–289.

Leary, P., Igel, H. & Ben-Zion, Y., 1991. Observation and modeling of fault zone seismic trapped waves in aid of precise evaluation of precursory microearthquake locations and evaluation, *Earthquake Prediction: State of the Art, Proc. Int. Conf.,* Strasbourg, France, 15–18 October 1991, 321–328.

Li, Y.G. & Leary, P., 1990. Fault zone seismic trapped waves, *Bull. seism. Soc. Am.,* **80,** 1245–1271.

Li, Y.G. & Vernon, F.L., 2001. Characterization of the San Jacinto fault zone near Anza, California, by fault zone trapped waves, *J. geophys. Res.,* **106,** 30 671–30 688.

Li, Y.G. & Vidale, J.E., 1996. Low-velocity fault-zone guided waves: numerical investigation of trapping efficiency, *Bull. seism. Soc. Am.,* **86,** 371–378.

Li, Y.G., Aki, K., Adams, D., Hasemi, A. & Lee, W.H.K., 1994. Seismic guided waves trapped in the fault zone of the Landers, California, earthquake of 1992, *J. geophys. Res.,* **99,** 11 705–11 722.

Li, Y.G., Aki, K., Vidale, J.E. & Alvarez, M.G., 1998. A delineation of the Nojima fault ruptured in the, *M* 7.2 Kobe, Japan, earthquake of 1995 using fault-zone trapped waves, *J. geophys. Res.,* **103,** 7247–7263.

Li, Y.G., Vidale, J.E., Aki, K. & Xu, F., 2000. Depth-dependent structure of the Landers fault zone using fault zone trapped waves generated by aftershocks, *J. geophys. Res.,* **105,** 6237–6254.

Marone, C. & Scholz, C.H., 1988. The depth of seismic faulting and the upper transition from stable to unstable regimes, *Geophys. Res. Lett.,* **15,** 621–624.

Michael, A.J. & Ben-Zion, Y., 1998. Inverting fault zone trapped waves with genetic algorithm, *EOS, Trans. Am. geophys. Un.,* **79,** F584.

Neal, L.A., Chester, J.S., Chester, F.M. & Wintsch, R.P., 2000. Internal structure of the Kern Canyon fault, California: a deeply exhumed strike-slip fault, *EOS, Trans. Am. geophys. Un.,* **81,** F1145.

Nishigami, K., Ando, M. & Tadokoro, K., 2001. Seismic observations in the DPRI 1800 m borehole drilled into the Nojima fault zone, south-west Japan, *Island Arc,* **10,** 288–295.

Peng, Z., Ben-Zion, Y., Michael, A.J. & Zhu, L., 2002. Quantitative analysis of seismic trapped waves in the rupture zone of the Landers, 1992, California earthquake: evidence for a shallow trapping structure, *EOS, Trans. Am. geophys. Un.,* **83,** F1069.

Reilinger, R.E. *et al.*, 1997. Global Positioning System measurements of the present day crustal movements in the Arabia–Africa–Eurasia plate collision zone, *J. geophys. Res.,* **102,** 9983–9999.

Rovelli, A., Caserta, A., Marra, F. & Ruggiero, V., 2002. Can seismic waves be trapped inside an inactive fault zone? The case study of Nocera Umbra, central Italy, *Bull. seism. Soc. Am.,* **92,** 2217–2232.

Schulz, S.E. & Evans, J.P., 2000. Mesoscopic structure of the Punchbowl fault, southern California and the geologic and geophysical structure of active strike slip faults, *J. Struct. Geol.,* **22,** 913, 930.

Seeber, L., Armbruster, J.G., Ozer, N., Aktar, M., Baris, S., Okaya, D., Ben-Zion, Y. & Field, E., 2000a. The 1999 Earthquake Sequence along the North Anatolia Transform at the juncture between the two main ruptures, in *The 1999 Izmit and Duzce Earthquakes: Preliminary Results,* pp. 209–223, ed. Barka *et al.*, Istanbul Technical University.

Seeber, L., Armbruster, J.G., Ozer, N., Ben-Zion, Y., Okaya, D., Peng, Z., Baris, S. & Aktar, M., 2000b. Seismogenic faulting at the juncture of the two *Mw*7+ 1999 ruptures of the North Anatolian transform in northwestern Turkey, *EOS, Trans. Am. geophys. Un.,* **81,** F836.

Sengor, A.M.C., Gorur, N. & Saroglu, F., 1985. Strike-slip faulting and related basin formation, in zones of tectonic escape: Turkey as a case study, in *Strike-Slip Faulting and Basin Formation: Society of Economic Paleontologists and Minerologists*, Vol. **37,** pp. 221–264, eds, Biddle, K.T. & Cristie Blick, N., Special Publication.

Shapiro, N.M., Campillo, M., Singh, S.K. & Pacheco, J., 1998. Seismic channel waves in the accretionary prism of the Middle America Trench, *Geophys. Res. Lett.,* **25,** 101–104.

Shapiro, N.M., Olsen, K.B. & Singh, S.K., 2000. Wave-guide effects in subduction zones: evidence from three-dimensional modeling, *Geophys. Res. Lett.,* **27,** 433–436.

Sibson, R.H., 1983. Continental fault structure and the shallow earthquake source, *J. geol. Soc. Lond.,* **140,** 747–767.

Spudich, P. & Olsen, K.B., 2001. Fault zone amplified waves as a possible seismic hazard along the Calaveras fault in central California, *Geophys. Res. Lett.,* **28,** 2533–2536.

Tarantola, A., 1987. *Inverse Problem Theory,* Elsevier, Amsterdam.

Taymaz, T., Jackson, J.A. & McKenzie, D., 1991. Active tectonics of the north and central Aegean sea, *Geophys. J. Int.* **106,** 433–490.

Toksöz, M.N., (ed.), 2002. The Izmit, Turkey, earthquake of 17 August 1999, *Bull. seism. Soc. Am.,* **92,** special issue.

Vidale, J.E., Helmberger, D.V. & Clayton, R.W., 1985. Finite-difference seismograms for *SH* waves, *Bull. seism. Soc. Am.,* **75,** 1765–1782.